

Essential Dynamics of Secondary Eyewall Formation

SERGIO F. ABARCA AND MICHAEL T. MONTGOMERY

Naval Postgraduate School, Monterey, California

(Manuscript received 21 November 2012, in final form 14 February 2013)

ABSTRACT

The authors conduct an analysis of the dynamics of secondary eyewall formation in two modeling frameworks to obtain a more complete understanding of the phenomenon. The first is a full-physics, three-dimensional mesoscale model in which the authors examine an idealized hurricane simulation that undergoes a canonical eyewall replacement cycle. Analysis of the mesoscale simulation shows that secondary eyewall formation occurs in a conditionally unstable environment, questioning the applicability of moist-neutral viewpoints and related mathematical formulations thereto for studying this process of tropical cyclone intensity change. The analysis offers also new evidence in support of a recent hypothesis that secondary eyewalls form via a progressive boundary layer control of the vortex dynamics in response to a radial broadening of the tangential wind field.

The second analysis framework is an axisymmetric, nonlinear, time-dependent, slab boundary layer model with radial diffusion. When this boundary layer model is forced with the aforementioned mesoscale model's radial profile of pressure at the top of the boundary layer, it generates a secondary tangential wind maximum consistent with that from the full-physics, mesoscale simulation. These findings demonstrate that the boundary layer dynamics alone are capable of developing secondary wind maxima without prescribed secondary heat sources and/or invocation of special inertial stability properties of the swirling flow either within or above the boundary layer. Finally, the time-dependent slab model reveals that the simulated secondary wind maximum contracts inward, as secondary eyewalls do in mesoscale models and in nature, pointing to a hitherto unrecognized role of unbalanced dynamics in the eyewall replacement cycle.

1. Introduction

Secondary eyewall formation (SEF) is widely recognized as an important research problem in the dynamics of mature tropical cyclones, but as of yet there is not a consensus on the phenomenon's fundamental physics. The conceptual and empirical linkage between secondary eyewalls (SEs) to hurricane intensity change (Willoughby et al. 1982, 1984; Kuo et al. 2008) and storm growth (Maclay et al. 2008) has fostered renewed interest in SEF (Houze et al. 2007), with substantial efforts currently under way in developing statistical forecasting tools for the operational community (Kossin and Sitkowski 2009). However, as of today, such forecasting instruments tend to rely more on empirical relations than in the understanding of the physical processes that lead to SEF.

Previous studies of the physics of SEF have summoned a variety of physical processes. These include the interaction of the tropical cyclone core with nearby weaker vorticity anomalies (Kuo et al. 2004, 2008); a finite-amplitude wind-induced surface heat exchange (WISHE; Emanuel 1994, 1995, 1997) instability triggered by external forcing, such as with the interaction of a tropical cyclone with a baroclinic eddy in the upper troposphere (e.g., Nong and Emanuel 2003); the hypothesized impact of vortex Rossby waves (VRWs) on the tropical cyclone inner core (Montgomery and Kallenbach 1997; Qiu et al. 2010; Martinez et al. 2010; Menelaou et al. 2012; Abarca and Corbosiero 2011), or anisotropic upscale energy cascades (Terwey and Montgomery 2008, hereafter TM08). It has been proposed recently that SEF results from high generation and accumulation of potential vorticity and that VRWs are not a contributing factor for SEF (Judt and Chen 2010). Another proposal is that the sustained latent heating outside the primary eyewall can lead to SEF (Rozoff et al. 2012) in association with a radial expansion of the kinetic energy and an increase of the axisymmetric efficiency

Corresponding author address: Dr. Sergio F. Abarca, Department of Meteorology, Naval Postgraduate School, Root Hall, Room 248, 589 Dyer Road, Monterey, CA 93943-5119.
E-mail: sfabarca@nps.edu

| Report Documentation Page | | Form Approved OMB No. 0704-0188 |
|---|----------------------|---|
| Public reporting burden for the collection of information is estimated to average 1 hour per response, including the time for reviewing instructions, searching existing data sources, gathering and maintaining the data needed, and completing and reviewing the collection of information. Send comments regarding this burden estimate or any other aspect of this collection of information, including suggestions for reducing this burden, to Washington Headquarters Services, Directorate for Information Operations and Reports, 1215 Jefferson Davis Highway, Suite 1204, Arlington VA 22202-4302. Respondents should be aware that notwithstanding any other provision of law, no person shall be subject to a penalty for failing to comply with a collection of information if it does not display a currently valid OMB control number. | | |
| 1. REPORT DATE OCT 2013 | 2. REPORT TYPE | 3. DATES COVERED 00-00-2013 to 00-00-2013 |
| 4. TITLE AND SUBTITLE Essential Dynamics of Secondary Eyewall Formation | | 5a. CONTRACT NUMBER |
| | | 5b. GRANT NUMBER |
| | | 5c. PROGRAM ELEMENT NUMBER |
| 6. AUTHOR(S) | 5d. PROJECT NUMBER | |
| | 5e. TASK NUMBER | |
| | 5f. WORK UNIT NUMBER | |
| 7. PERFORMING ORGANIZATION NAME(S) AND ADDRESS(ES) Naval Postgraduate School (NPS), Department of Meteorology, Monterey, CA, 93943 | | 8. PERFORMING ORGANIZATION REPORT NUMBER |
| 9. SPONSORING/MONITORING AGENCY NAME(S) AND ADDRESS(ES) | | 10. SPONSOR/MONITOR'S ACRONYM(S) |
| | | 11. SPONSOR/MONITOR'S REPORT NUMBER(S) |
| 12. DISTRIBUTION/AVAILABILITY STATEMENT Approved for public release; distribution unlimited | | |
| 13. SUPPLEMENTARY NOTES | | |
| 14. ABSTRACT <p>The authors conduct an analysis of the dynamics of secondary eyewall formation in two modeling frameworks to obtain a more complete understanding of the phenomenon. The first is a full-physics, threedimensional mesoscale model in which the authors examine an idealized hurricane simulation that undergoes a canonical eyewall replacement cycle. Analysis of the mesoscale simulation shows that secondary eyewall formation occurs in a conditionally unstable environment, questioning the applicability of moistneutral viewpoints and related mathematical formulations thereto for studying this process of tropical cyclone intensity change. The analysis offers also new evidence in support of a recent hypothesis that secondary eyewalls form via a progressive boundary layer control of the vortex dynamics in response to a radial broadening of the tangential wind field. The second analysis framework is an axisymmetric, nonlinear, time-dependent, slab boundary layer model with radial diffusion. When this boundary layer model is forced with the aforementioned mesoscale model's radial profile of pressure at the top of the boundary layer, it generates a secondary tangential wind maximum consistent with that from the full-physics, mesoscale simulation. These findings demonstrate that the boundary layer dynamics alone are capable of developing secondary wind maxima without prescribed secondary heat sources and/or invocation of special inertial stability properties of the swirling flow either within or above the boundary layer. Finally, the time-dependent slab model reveals that the simulated secondary wind maximum contracts inward, as secondary eyewalls do in mesoscale models and in nature, pointing to a hitherto unrecognized role of unbalanced dynamics in the eyewall replacement cycle.</p> | | |
| 15. SUBJECT TERMS | | |

| | | | | | |
|----------------------------------|------------------------------------|-------------------------------------|--|-------------------------------------|------------------------------------|
| 16. SECURITY CLASSIFICATION OF: | | | 17. LIMITATION OF ABSTRACT Same as Report (SAR) | 18. NUMBER OF PAGES 15 | 19a. NAME OF RESPONSIBLE PERSON |
| a. REPORT unclassified | b. ABSTRACT unclassified | c. THIS PAGE unclassified | | | |

there as defined by Schubert and Hack (1982) and Hack and Schubert (1986).

Only recently has a clear dynamical link been made between the overarching mechanisms of tropical cyclone intensification and the physics of SEF (Huang et al. 2012). This realization followed soon after the development of the paradigm-shifting study of Smith et al. (2009), in which it was shown that, from the perspective of the azimuthally averaged system-scale flow, the spinup of the swirling circulation occurs via two mechanisms.

The first spinup mechanism occurs above the frictional boundary layer by the conventional picture of inflowing rings of fluid that (approximately) materially conserve their azimuthally averaged absolute angular momentum $M = rv + (1/2)fr^2$, where r is the radius from the circulation center, v is the azimuthally averaged tangential velocity, and f is the Coriolis parameter. The inflowing air occurs primarily below the midtroposphere and results from the radial gradient of buoyancy generation rate associated with the aggregate positive latent heating in the deep convective clouds that span the troposphere. The latent heating rate of these clouds is maximized near the midtroposphere (~ 7 km). Since the frictional torque on fluid rings above the boundary layer is negligible, and assuming pressure torques from horizontal eddy motions are negligible, M will be materially conserved there. Then, the foregoing relationship between M and v implies that as deep convection draws in rings of fluid, the tangential velocity will increase. This mechanism has been articulated previously by many authors (e.g., Ooyama 1969; Carrier 1971a; Willoughby 1979; Shapiro and Willoughby 1982; Willoughby 1995). Using a non-hydrostatic, convection-representing model, recent work has affirmed that this mechanism may be interpreted in terms of axisymmetric balance dynamics and has used this mechanism to explain why the vortex expands in size (Smith et al. 2009; Bui et al. 2009; Fudeyasu and Wang 2011).

The second spinup mechanism occurs within the frictional boundary layer,¹ when the depletion of M by nonconservative forces is surpassed by the inward radial advection of M associated with the strong frictional inflow. Although M is not materially conserved in the boundary layer, positive tangential wind tendency (resulting

in large tangential wind velocity) can be achieved there if the radial inflow is sufficiently large to bring the air parcels to small radii with minimal loss of M . This spinup mechanism, while coupled to the interior flow via the radial pressure gradient at the top of the boundary layer, is tied fundamentally to the dynamics of the boundary layer, where the flow is not in gradient wind balance over a substantial radial span (Smith et al. 2009; Smith and Montgomery 2010). Whereas this second mechanism cannot be captured by axisymmetric balance dynamics, numerical model studies and recent observations show it to be the essential pathway for the generation of the maximum tangential winds on the cyclone scale (Zhang et al. 2001; Smith et al. 2009; Smith and Thomsen 2010; Sanger et al. 2013).²

Motivated by these developments, using the model–observation-consistent dataset of Wu et al. (2012), Huang et al. (2012) proposed that the boundary layer force imbalance in the radial direction and its radial structure play in an important role in initiating and sustaining convective activity radially outward of the primary eyewall. They were the first to conceptualize and demonstrate SEF as the culmination of a sequence of structural changes in a mature hurricane. According to the new model, the sequence begins with a broadening of the tangential wind field (via the first spinup mechanism) followed by an increase of boundary layer inflow outside of the primary eyewall and the development of supergradient winds in this region near the top of the boundary layer. The latter is associated with horizontal convergence and the emergence of the deep convection that form the roots of the SE. They suggested also that simple diagnostics involving the agradient force could prove helpful in operational practice to help diagnose SEF.

In the context of the new SEF model, we believe it is useful to further analyze SEF in the idealized full-physics, three-dimensional simulation generated by TM08. Although the TM08 simulation was used originally to explore the hypothesis of anisotropic inverse cascades mentioned previously, this same simulation will be used here to test the new model advanced by Huang et al. (2012). Since this simulation has been further demonstrated to furnish a canonical SE (Terwey et al. 2013), the simulation is believed to be an ideal laboratory for such a test. Because boundary layer dynamics are hypothesized to be a central ingredient in both the establishment of convective activity and the emergence of a secondary wind maximum, the TM08 simulation will be used in conjunction with a simple slab boundary layer

¹ In this paper we follow Smith et al. (2009) and Smith and Montgomery (2010) and adopt a dynamical definition of the boundary layer, using the term “boundary layer” to describe the shallow layer of relatively strong inflow near the sea surface and that arises largely because of the frictional disruption of gradient wind balance near the surface. It will be shown below for the numerical simulation analyzed in detail here that the boundary layer so defined is about 1 km deep in the primary eyewall region of the hurricane and somewhat deeper (~ 1.5 km) in the region of SEF.

² A review of the most prominent tropical cyclone intensification paradigms over the past five decades is presented by Montgomery and Smith (2013).

model to isolate the pure boundary layer response to an imposed wind field at the top of the boundary layer.

An outline of the remaining parts of the paper is as follows: Section 2 describes the two numerical models used in this study and summarizes the analysis methodology employed. Section 3 reviews the evidence of the canonical SE in the TM08 simulation. Section 4 presents kinematic characteristics of the SEF event. Section 5 presents a dynamical analysis of the SEF event. Section 6 uses the tangential wind at the top of the simulated boundary to compare the predictions between the slab boundary layer model and the TM08 simulation. Section 7 presents our conclusions.

2. Models and methodology

a. The mesoscale model

This paper analyzes the SEF simulation initially studied by TM08 and recently revisited by Terwey et al. (2013) that used the Regional Atmospheric Modeling System (RAMS; Pielke et al. 1992; Cotton et al. 2003). Briefly, RAMS is a three-dimensional, nonhydrostatic numerical modeling system with two-way interactive nesting capabilities (Clark and Farley 1984). The model simulation uses a surface flux parameterization for momentum and heat based on the Louis (1979) scheme; the radiation scheme, which includes cloud microphysical interactions, introduced by Harrington (1997); the subgrid-scale turbulence scheme, based on Smagorinsky (1963) and that incorporates the modifications from Lilly (1962) and Hill (1974); and the microphysical scheme, with seven species of hydrometeors by Walko et al. (1995).

The RAMS simulation is an idealized integration on an f plane (centered at 15°N), with constant sea surface temperature of 28°C. The simulation is configured with 30 vertical levels with vertical grid spacing varying gradually from 300 m near the surface to 1800 m near the top of the domain (at about 26-km altitude). The horizontal grid structure is nested on three domains, with horizontal grid spacings of 24, 6, and 2 km and 168, 170, and 251 grid points, respectively. The respective domain sizes are 4032, 1020, and 502 km. Each inner grid is located at the center of the parent grid. The outermost grid is cyclic in the horizontal direction (to help constrain mass conservation in the domain). Given the size of the largest domain and the relatively small size of the simulated vortex, it is thought that there is minimal interaction of the storm with itself (TM08).

The simulation is initialized with a quiescent environment in which the vertical thermodynamic structure is given by Jordan's (1958) summertime Caribbean sounding. The initial vortex employed is a weak (10 m s^{-1})

mesoscale cyclonic vortex in gradient and hydrostatic balance, located at the center of the three domains. The initial vortex reaches its maximum tangential wind velocity at 4-km height and has a radius of maximum winds (RMW) of 75 km. The initial conditions include also a positive moisture anomaly with a monotonic increase in water vapor mixing ratio by 1.3 g kg^{-1} from the environment to the center of the initial vortex. Further details of the RAMS simulation and the experimental setup can be found in TM08 and in Montgomery et al. (2006).

Throughout this study we present azimuthal averages of the simulated variables. The averages are obtained after interpolating the RAMS data from its original Arakawa C grid in Cartesian coordinates into a cylindrical grid, whose center is determined as the centroid of the potential vorticity field in the lowest 7.3 km of the domain. All of the results presented for specific times correspond to 2-h averages, centered at the noted time. For the present analysis, temporal averages are preferred over instantaneous fields because the time-averaging procedure reduces the effects of transient flow features, such as inertia-gravity waves and individual convective cells that are common features in the analyzed dataset.

b. The time-dependent boundary layer model

To address the question of whether boundary layers can generate secondary wind maxima in response to an imposed hurricane wind field above without secondary wind maxima, a slab boundary layer model, based on that described in Shapiro (1983), is integrated in radius and time. The model solves the following cylindrical radial and tangential momentum equations:

$$\begin{aligned} \frac{\partial \langle u \rangle}{\partial t} = & -\langle u \rangle \frac{\partial \langle u \rangle}{\partial r} + \frac{\langle v \rangle^2}{r} + f \langle v \rangle - \frac{C_D}{h} \langle u \rangle (\langle u \rangle^2 + \langle v \rangle^2)^{1/2} \\ & - K \left(\nabla^2 \langle u \rangle - \frac{\langle u \rangle}{r^2} \right) - \frac{1}{\rho} \frac{\partial \langle p \rangle}{\partial r}, \end{aligned} \quad (1)$$

$$\begin{aligned} \frac{\partial \langle v \rangle}{\partial t} = & -\langle u \rangle \frac{\partial \langle v \rangle}{\partial r} - \langle u \rangle \frac{\langle v \rangle}{r} - f \langle u \rangle - \frac{C_D}{h} \langle v \rangle (\langle u \rangle^2 + \langle v \rangle^2)^{1/2} \\ & - K \left(\nabla^2 \langle v \rangle - \frac{\langle v \rangle}{r^2} \right), \end{aligned} \quad (2)$$

where u and v are the radial and tangential wind velocities, z is the vertical coordinate, t is time, ρ is the air density, p is pressure, C_D is the drag coefficient, h is the prescribed constant boundary layer height, ∇^2 is the horizontal Laplacian operator in cylindrical coordinates, K is the horizontal eddy diffusivity, angle brackets denote azimuthal average, and the rest of the symbols have their

standard meanings. In Eqs. (1) and (2), the terms on the left-hand side are the local time rate of change of the radial and tangential velocity components, and those on the right-hand side are, from left to right, respectively, radial advection, centrifugal, Coriolis, frictional, and radial diffusion forces. The radial momentum equation [Eq. (1)] contains also the radial pressure gradient force, which is the driving force for the boundary layer flow. For simplicity, the slab model neglects vertical advection (Shapiro 1983).

As is standard in boundary layer calculations (e.g., Smith 1968; Carrier 1971b), the tangential wind at boundary layer top is used to force the slab boundary layer model through the radial pressure gradient term in Eq. (1). The tangential wind at boundary layer top is assumed to be in gradient wind balance with the pressure field.

To complete the specification of the slab model a suitable formulation of the surface drag coefficient is required. After the observational study of Bell et al. (2012a), based on the Coupled Boundary-Layer Air–Sea Transfer experiment (CBLAST; Black et al. 2007; Drennan et al. 2007; French et al. 2007; Zhang et al. 2008), we compute the surface drag coefficient following Thomsen et al. (2013) as $C_D = 0.7 \times 10^{-3} + 1.4 \times 10^{-3} [1 - \exp(-0.055|\mathbf{u}|)]$.³ For the integrations presented here, a constant radial eddy diffusivity of $K = 1 \times 10^4 \text{ m}^2 \text{ s}^{-1}$ is used. This relatively large value is chosen as a crude, but plausible, parameterization of the shear instability and mixing processes at the inner edge of the eyewall. This diffusivity serves also to regularize the numerical boundary layer solution that, in the absence of radial momentum diffusion, tends to produce discontinuous “shocks” in both the radial and tangential velocity fields near and just outside the RMW (Shapiro 1983).

The magnitude of the chosen radial eddy diffusivity is not unlike the values estimated from in situ observations by Zhang and Montgomery (2012), who reported values as high as $K = 3.43 \times 10^3 \text{ m}^2 \text{ s}^{-1}$ (their Table 1) in Hurricane David (1979). The magnitude of the radial eddy diffusivity is comparable also to that used by Rotunno and Emanuel (1987, their section 3a) in their axisymmetric modeling study (attaining values as large as $1 \times 10^4 \text{ m}^2 \text{ s}^{-1}$). Qualitatively similar slab boundary results to that described below are obtained with decreased eddy diffusivities as low as $6 \times 10^3 \text{ m}^2 \text{ s}^{-1}$.

The model is integrated in time and radius, employing a constant Coriolis parameter evaluated at 15°N to

match the value used in the RAMS simulation. A constant boundary layer depth of 2 km is used to be broadly consistent with the boundary layer depth in the region of SEF diagnosed from the RAMS simulation (see upcoming Figs. 2a–c and discussion). With the given choices of C_D and h , the vertically averaged slab boundary layer drag force magnitude in the tangential direction (between 75 and 150 km of radius) is $2.41 \times 10^{-3} \text{ m s}^{-2}$. In comparison, the vertically averaged tangential drag force in the RAMS simulation (calculated as the residual of the average forces in the lowest 1138 m, between 75- and 150-km radius, at hour 23—during SEF, as shown later) has a magnitude of $1.38 \times 10^{-3} \text{ m s}^{-2}$, with local values reaching magnitudes of $5.00 \times 10^{-3} \text{ m s}^{-2}$. In other words, the magnitude of the tangential frictional force, as well as the rest of the parameter choices in the slab boundary layer model, falls within the range of values obtained in the RAMS simulation.

3. Secondary eyewall in the RAMS simulation

To set the scene for the upcoming diagnostic analyses, we review first the main evidence of SEF in the TM08 simulation. Figure 2 of TM08 presents a time series of minimum pressure, RMW (at the lowest model level of 147 m), and maximum azimuthal-mean tangential winds (at 1 km) for the 220-h numerical simulation. The simulated storm evolves from a weak mesoscale convective vortex to a mature hurricane that subsequently undergoes a canonical eyewall replacement cycle. In the figure, SEF is characterized by a sudden expansion of the RMW (from radius 35 to 80 km right before hour 180), which is associated with a weakening of the tangential wind in the primary eyewall and an intensification of the tangential wind in the SEF radial region. Following TM08, we denote hour 156 as hour 0 to more easily describe the kinematics and dynamics of SEF.

Figure 1 shows radius–time diagrams of the azimuthal-mean tangential and vertical velocity at a height of 1512 m from the TM08 simulation. Although similar to Fig. 2 in Terwey et al. (2013), this figure plots the evolution of the tangential and vertical velocity at the height of maximum tangential winds in the region where the secondary eyewall first becomes apparent in the azimuthally averaged fields. As discussed in Terwey et al. (2013), Fig. 1 further evidences that the analyzed simulation exhibits a canonical eyewall replacement cycle as inferred from observations (e.g., Willoughby et al. 1982; Houze et al. 2007; Bell et al. 2012b; Sitkowski et al. 2012). The RAMS simulation is consistent also with realistic numerical integrations of hurricanes that exhibit secondary eyewalls (e.g., Judt and Chen 2010; Abarca

³ Sensitivity analysis using the Deacon’s formula (Roll 1965) and a constant $C_D = 2.0 \times 10^{-3}$ demonstrate robustness of the results, with strong qualitative and quantitative agreement among a corresponding suite of integrations (not shown).

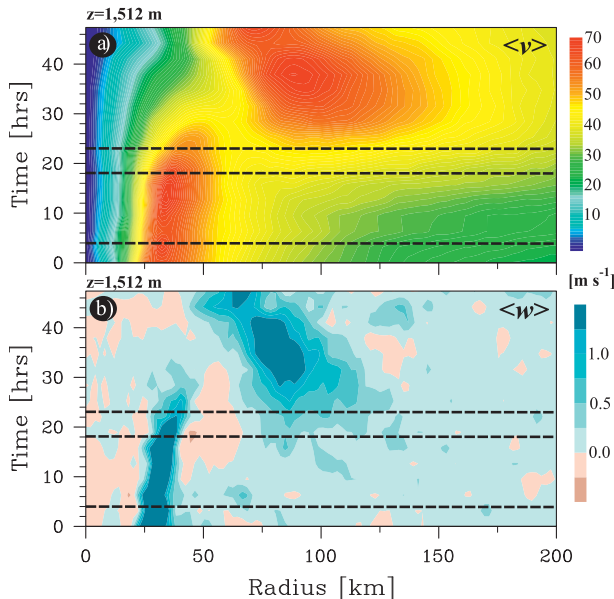


FIG. 1. Radius–time plot of (a) azimuthally averaged tangential velocity (m s^{-1}) and (b) azimuthally averaged vertical velocity (m s^{-1}) within 200-km radius from vortex center from the meso-scale model simulation. Panels are shown at 1512-m height, where the strongest azimuthally averaged tangential winds are found. Dashed lines highlight the three times during the secondary eyewall formation process used often in the subsequent analysis.

and Corbosiero 2011; Zhou and Wang 2011; Zhou et al. 2011; Rozoff et al. 2012). Specifically, at a height of 1512 m, the primary eyewall is centered around 34-km radius and its tangential wind intensifies up to hour 15 (Fig. 1a). Subsequently, these tangential winds weaken monotonically from 80.9 m s^{-1} at hour 15 to 26.5 m s^{-1} at hour 42. As the strengthening and weakening occurs in the primary eyewall, the tangential winds outside the primary eyewall undergo a progressive amplification on a relatively broad scale that extends beyond the domain shown ($>200 \text{ km}$). This amplification accounts for the radial expansion of the swirling wind field reported previously in SEF studies (e.g., Huang et al. 2012; Rozoff et al. 2012). Superimposed on this broadening of the tangential wind, a more localized tangential wind maximum emerges first around hour 19 at 85-km radius and then subsequently at later times and at other model heights [discussed further in section 5 and in Terwey et al. (2013)]. This localized wind maximum continues to intensify, and exceeds the interior tangential wind maximum at about hour 25 (Fig. 2 of TM08). The new wind maximum further intensifies and contracts slowly inward, thereby completing an eyewall replacement cycle.

Figure 1b shows the evolution of the azimuthally averaged vertical velocity field. The strongest vertical velocities attain values somewhat larger than 1.5 m s^{-1} and

are located in the regions of strongest tangential winds (Fig. 1a) associated with the primary and secondary eyewalls. As the tangential wind velocity of the primary eyewall weakens (Fig. 1a), so does the corresponding vertical velocity (Fig. 1b). In Fig. 1b, the emergence of the secondary eyewall is reflected in the establishment of a maximum of azimuthal-mean vertical velocity that occurs at nearly the same time as the development of the localized tangential wind maximum (Fig. 1a). However, near the 85-km radius the initial mean secondary updraft maximum can be recognized as early as hour 15—about 4 h before the emergence of the secondary tangential wind maximum at 1512-m height. In addition to showing the demise of the primary eyewall and the emergence of the secondary eyewall, Fig. 1b shows the so-called moat—a region of pronounced subsidence and greatly diminished radar reflectivity (Houze et al. 2007) that is clearly discernable between the two eyewalls. The subsiding mean motion attains magnitudes greater than 0.5 m s^{-1} at hour 18 near the 48-km radius.

4. Secondary eyewall formation kinematics

Figure 2 shows the height–radius structure of the azimuthally averaged radial velocity $\langle u \rangle$, tangential velocity $\langle v \rangle$, and vertical velocity $\langle w \rangle$ within 200 km of the circulation center during the SEF period. This region encompasses both the primary and secondary eyewalls. The panels highlight characteristic features of the azimuthally averaged horizontal and vertical velocity fields that are found during the 24-h period in which high-time-resolution output is available.

Figures 2a–c show that strong inflow is confined to the lowest km, with the largest values at the lowest model level ($z = 147.64 \text{ m}$). Initially, the strongest values of inflow are located just outside the RMW of the primary eyewall. This inflow exceeds 25 m s^{-1} at 30-km radius at hour 4 and 20 m s^{-1} at 35-km radius at hour 18. Besides the maximum inflow associated with the primary eyewall ($>15 \text{ m s}^{-1}$), another inflow maximum progressively emerges in association with the SEF shown in Fig. 1. The second inflow maximum is centered at about 80-km radius at 18 h (Fig. 2b) and gradually becomes the strongest in the domain, exceeding 20 m s^{-1} at hour 23 (Fig. 2c).

Figures 2a–c show that the main outflow resides at upper levels (between 11- and 15-km height) and radially exterior to the eyewall regions. At early times (Fig. 2a), when the storm is characterized by one eyewall (Fig. 1), the strongest outflow is more vertically confined than at later times (Fig. 2c), when the nascent secondary eyewall projects into the azimuthally averaged flow (Fig. 1). In addition to the upper-level outflow, Figs. 2a–c show also secondary outflow regions located directly above

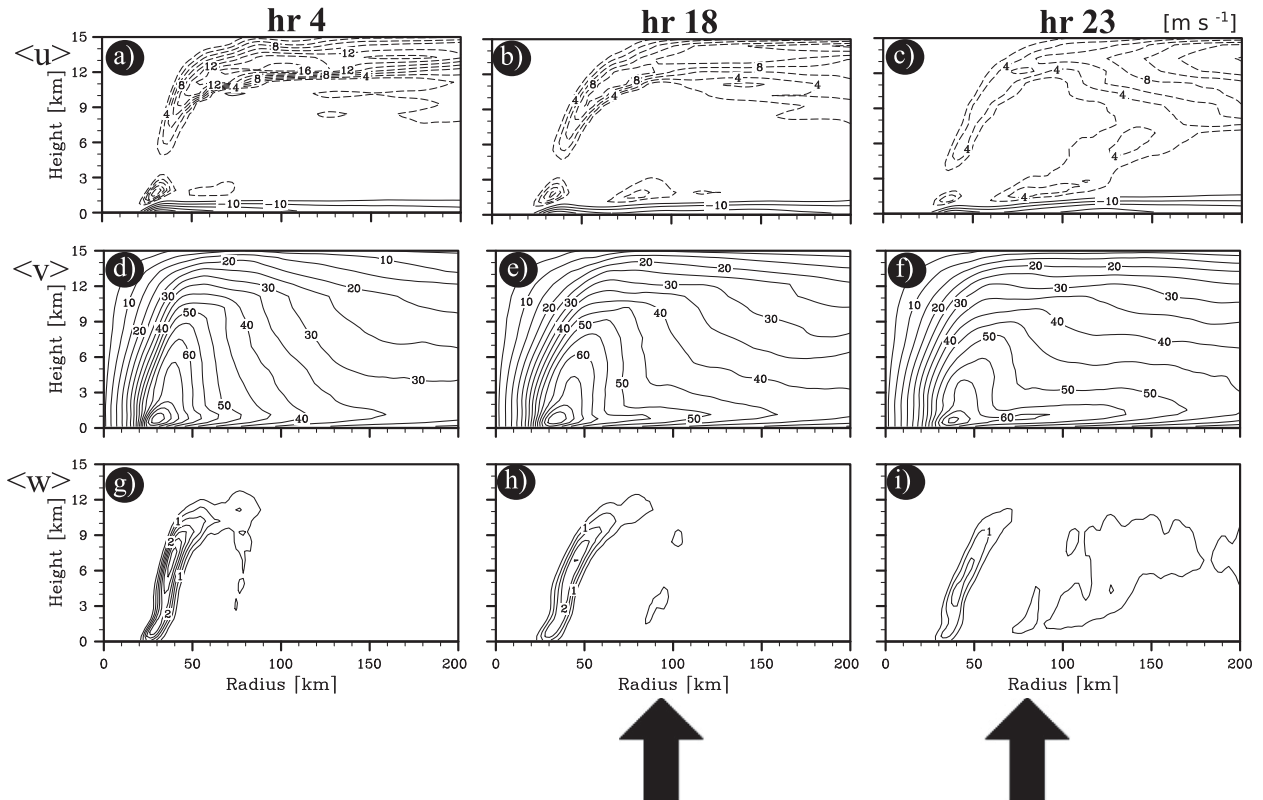


FIG. 2. The 2-h and azimuthal average of (a)–(c) radial, (d)–(f) azimuthal, and (g)–(i) vertical wind components (m s^{-1}), centered at (left) hour 4, (middle) hour 18, and (right) hour 23 from the mesoscale model simulation of TM08. Contours are plotted every 5 (0.5) m s^{-1} for the azimuthal and radial (vertical) wind velocities, except for negative contours in the radial wind, which are plotted every 2 m s^{-1} . Dashed lines indicate positive (negative) values in the radial (vertical) wind component. The zero contour is not plotted. Vertical arrows denote the approximate radius of SEF at hours 18 and 23, as defined by the secondary maximum in vertical velocity in (h),(i).

the inflow maxima. As the primary eyewall weakens, the lower-tropospheric outflow associated with the primary eyewall decreases in magnitude from about 10 m s^{-1} at hour 4 to about 8 m s^{-1} at hour 18 and to less than 5 m s^{-1} at hour 23. In the meantime, the lower-tropospheric outflow associated with the SE increases in magnitude with time, and by hour 18 this outflow exceeds 4 m s^{-1} (Fig. 2b).

Figure 2d shows that the tangential velocity structure at hour 4 bears a strong resemblance to a major tropical cyclone as observed with high-resolution dropsonde data (e.g., Montgomery et al. 2006; Bell and Montgomery 2008). The tangential wind attains its maximum value near the top of the boundary layer (cf. Fig. 1a) and gradually weakens with height and radius. The tangential wind structure of Fig. 2d evolves to a configuration where a secondary maximum is discernable between 70- and 90-km radius at hour 23 (Fig. 2f). This structure change is associated with a progressive radial broadening of the tangential wind field and the subsequent development of a secondary tangential wind maximum (Fig. 1). The broadening of the tangential wind field occurs throughout the troposphere and is

illustrated by inspecting the 30 and 40 m s^{-1} contours and observing their progressive movement upward and outwards with time (Figs. 2d–f). Another notable feature is that the development of the secondary tangential wind maximum occurs near the top of the inflow layer (illustrated by examining the evolution of the 60 m s^{-1} contour in Fig. 2f).

Figure 2g shows $\langle w \rangle$ at hour 4. At this time the vertical motion is confined mostly to the primary eyewall in a relatively narrow radial region centered at about 30-km radius and sloping outward to about 45-km radius at 9-km height. At later times the vertical velocity structure of Fig. 2g changes qualitatively to a configuration with a clear secondary maximum outside the primary eyewall (Fig. 2i). As the secondary eyewall forms, a secondary maximum of vertical velocity emerges (Fig. 2h) and strengthens (Fig. 2i) above the region of strongest tangential (Figs. 2e,f) and radial (Figs. 2b,c) winds. At early times, the projection onto the azimuthally averaged vertical velocity in the nascent secondary eyewall occupies a broader radial region and possesses a weaker magnitude than the primary eyewall. The difference in the mean

vertical velocity structure between the two eyewalls may be explained by the fact that the convective activity in the secondary eyewall occupies a broader radial region and is not contiguous in azimuth (see Fig. 4 of TM08).

During the time when the primary eyewall tangential winds are strengthening, Fig. 2g shows that the azimuthally averaged vertical velocity exhibits two distinct maxima: one near the top of the inflow layer and another one in the middle troposphere (centered at about 6.5-km height). As the primary eyewall weakens, the maximum near the top of the inflow layer disappears. However, as the secondary eyewall emerges, the two maxima in the emerging eyewall are evident in Figs. 2h and 2i. The midtropospheric updraft maximum has been related to the aggregate radial gradient of the buoyancy generation rate resulting from the latent heat release in the deep cumulus convection in the central region of the vortex (Hendricks et al. 2004; Montgomery et al. 2006, 2009; Bui et al. 2009). The lower updraft maximum has been identified with boundary layer inertial effects in a radial region where boundary layer inflow terminates (Smith et al. 2009). The next section presents dynamical evidence that the lower-level updraft maximum is indeed associated with inertial effects, as is the tangential wind acceleration near the top of the BL and the emergence of the SE itself.

5. Secondary eyewall formation dynamics

The objective of this section is to obtain a more complete understanding of the thermodynamical and dynamical processes contributing to SEF. We begin the analysis with an examination of the structure and evolution of the azimuthally averaged surfaces of equivalent potential temperature θ_e and M . This will furnish a zero-order view of the thermodynamical pathway to SEF in the RAMS model. The illustrated evolution of the low-level M surfaces, together with the analysis in sections 3 and 4, then motivates an analysis of departures of gradient wind balance and a quantification of the various flow contributions to the tangential wind tendency during the SEF process.

a. Evolution of θ_e and M surfaces

Figure 3 presents radius–height plots of azimuthal and 2-h averages of θ_e , [calculated using Eq. (43) in Bolton (1980)] and M centered at hours 4, 18, and 23, as the secondary eyewall forms. These quantities are particularly informative since they are approximately conserved following moist air parcels in the free atmosphere assuming the azimuthal pressure torque and small-scale mixing processes are negligible.

Figure 3a affirms broadly the expected pattern of θ_e within a tropical cyclone (Hawkins and Imbembo 1976;

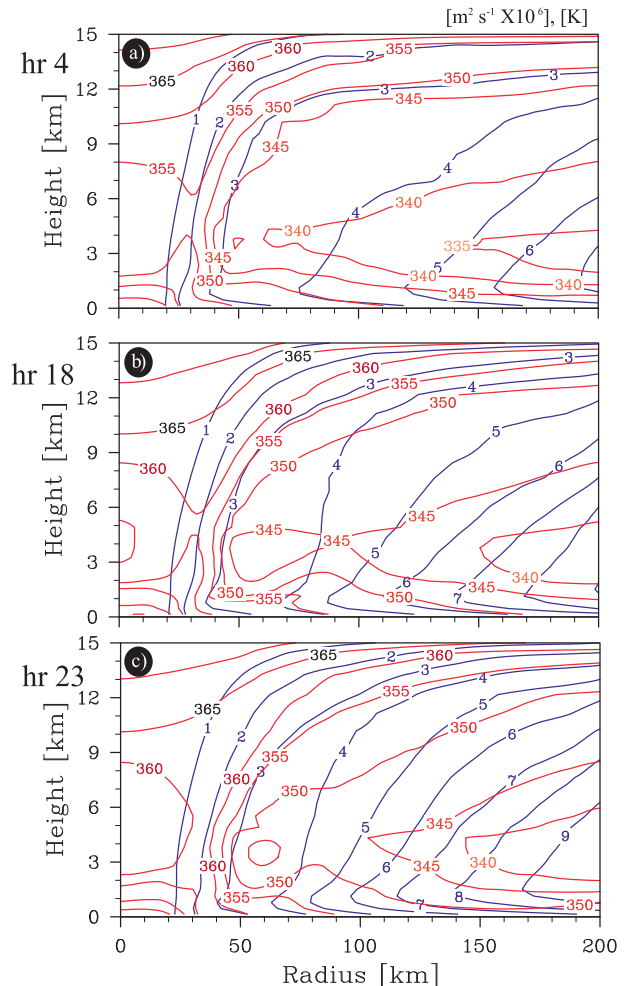


FIG. 3. The 2-h and azimuthal average of absolute angular momentum ($\text{m}^2 \text{s}^{-1} \times 10^6$) and equivalent potential temperature (K) within 200 km of vortex center from the mesoscale model simulation. Plots are centered at (a) hour 4, (b) hour 18, and (c) hour 23. Contours are plotted every $1 \text{ m}^2 \text{s}^{-1} \times 10^6$ and 5 K. See text for details.

Bogner et al. 2000), with a markedly different structure of the θ_e isopleths in the inner core and radially outward of it. In the radial region where SEF takes place, and particularly at radii greater than about 75 km, the θ_e surfaces are approximately horizontal. In that radial region there is a decrease of θ_e with height from the surface up to about 3-km height (indicating that, given lifting and saturation, the lower troposphere is convectively unstable in the azimuthal mean). Above 3-km height, in that same radial region, there is an increase of θ_e with height (implying that, given lifting to saturation, the lower troposphere is, in the azimuthal mean, convective unstable). Closer to the center, in the vicinity of the primary eyewall, the θ_e isopleths change their pattern by increasing their magnitude radially inward and exhibiting a structure weakly slanted from vertical

below about 6 km. Above 6-km height, the θ_e isopleths lean upward and outward. Since θ_e is essentially conserved above the boundary layer, the upward and outward pattern of the θ_e isopleths results from the upward and outward flow of the primary eyewall (Fig. 2a). Radially inward of the primary eyewall, and as a result of strong subsidence in the eye, θ_e isopleths exhibit a radius–height structure similar to that found radially outside of the eyewall. As the secondary eyewall forms, the vertical motions are increasingly projecting into the azimuthal average (Figs. 2h,i) and the azimuthally averaged θ_e isopleths start to lean upward and outward between 70- and 140-km radius.

The structure and evolution of M isopleths offer dynamical insight into the SEF process. Above the boundary layer where there is an absence of strong diffusion, the inward migration of the M isopleths indicates an amplification of the swirling wind field as discussed in the introduction.⁴ A comparison of Figs. 3a–c evidences that the largest inward displacement of M isopleths occurs near the top of the inflow layer (Figs. 2a–c). The top of the strong inflow is where the strongest tangential wind velocities are observed and where the secondary tangential wind maximum emerges (Figs. 2d–f). Near the ocean surface, the M surfaces tilt strongly inward with height. This inward tilt implies that the tangential wind increases with height and that M is being diffused into the ocean surface by nonconservative processes. Near the surface, the tangential wind is subgradient relative to the gradient wind near the top of the boundary layer. Above the innermost point of each M surface, the M surfaces tilt outward with height. The outward tilt is consistent with the ascent of air out of the boundary layer and its flaring out to large radius in the upper troposphere (Fig. 2). The fact that the secondary eyewall tangential maximum develops near the top of the BL (Fig. 2d–f) suggests plausibly that the spinup of the secondary eyewall may be intimately linked with the underlying boundary layer dynamics, as initially proposed by Huang et al. (2012).

Finally, in the primary eyewall (Figs. 2g–i), the isopleths of θ_e and M are nearly congruent throughout the troposphere, with the θ_e surfaces sloping radially outward. This configuration indicates that the circulation tends to be conditionally symmetrically neutral (Emanuel 1986). However, in the region of SEF, the θ_e and M isopleths are not congruent and intersect one another, with the θ_e surfaces being approximately

horizontal. The evolution of the θ_e and M surfaces demonstrate that the secondary eyewall as simulated here does not form via a pathway of moist-neutral convective dynamics (cf. Nong and Emanuel 2003) and points to an intensification process (Nguyen et al. 2008; Montgomery et al. 2009; Smith et al. 2009) that is not captured by the conceptual and modeling framework of moist-neutral dynamics as described in Emanuel (1986, 1994, 1995, 1997, 2004).

b. Departures of balance in the boundary layer

To further understand the boundary layer dynamics that contribute to the formation and spinup of the secondary eyewall, we consider first an analysis of the agradiant force followed by an analysis of the various flow contributions to the spinup of the tangential wind in the boundary layer and above. The agradiant force per unit mass is defined as the difference between the local radial pressure gradient and the sum of the centrifugal and Coriolis forces in the radial momentum equation (Smith et al. 2009 and Huang et al. 2012):

$$\text{Agradiant Force} = -\frac{1}{\langle \rho \rangle} \frac{\partial \langle p \rangle}{\partial r} + \frac{\langle v \rangle^2}{r} + f \langle v \rangle, \quad (3)$$

where the symbols are as defined earlier. The agradiant force is a diagnostic of the departure of axisymmetric gradient wind balance in the radial coordinate direction. A positive agradiant force implies an outward-directed acceleration and occurs when the tangential wind is supergradient. A negative agradiant force implies an inward-directed acceleration and occurs when the flow is subgradient. Supergradient flow indicates that the tangential wind is larger than necessary to satisfy gradient wind balance, while subgradient flow indicates that the tangential wind is smaller than necessary to satisfy gradient wind balance.

Figure 4 shows radius–height plots of agradiant-force isopleths centered at 4, 18, and 23 h. At all times shown the figure indicates that departures of gradient wind balance occur predominantly around the declining primary eyewall and the emerging secondary eyewall (Fig. 2). Supergradient winds attain their maximum values near the top of the inflow layer (Figs. 2a–c) and are collocated with the strongest tangential winds (Figs. 2d–f) and the largest inward displacement of the M isopleths (Figs. 3a–c). As the SE forms, the agradiant force progressively increases in magnitude.⁵ Specifically, at hour 4 and 80-km radius, the largest

⁴ Assuming, as discussed in the introduction and shown further below, that asymmetric eddy processes are small and can be ignored to a first approximation.

⁵ Consideration of a generalized Ekman imbalance will render consistent results with those presented here, since the radial frictional force in the inflow layer is directed radially outward.

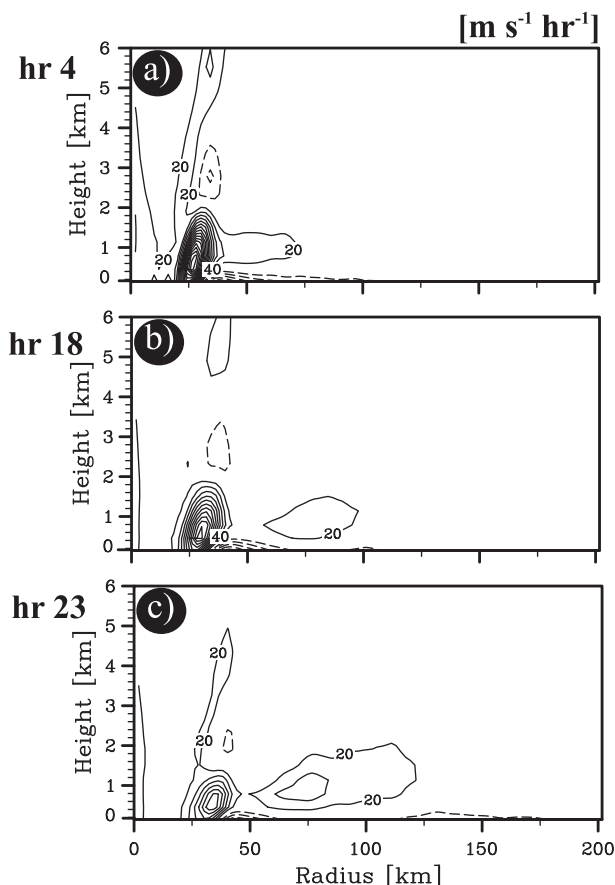


FIG. 4. The 2-h and azimuthal average of gradient force ($\text{m s}^{-1} \text{h}^{-1}$) within 200 km of vortex center from the mesoscale simulation. Plots are centered at (a) hour 4, (b) hour 18, and (c) hour 23. Contours are plotted every $20 \text{ m s}^{-1} \text{h}^{-1}$. See text for details.

agradient acceleration is about $16 \text{ m s}^{-1} \text{h}^{-1}$, and at hour 23, it surpasses $40 \text{ m s}^{-1} \text{h}^{-1}$. Thus, subgradient flow is found radially outwards of the regions with largest values of supergradient flow and at the lowest level of the domain (where friction is the largest).

The results presented in Fig. 4 support the findings and interpretations of Huang et al. (2012) by confirming that the supergradient flow increases progressively within and near the top of the boundary layer as the secondary wind maximum emerges. To further test the proposed boundary layer control hypothesis, we carry out next a diagnosis of the various flow contributions to the tangential velocity tendency equation during the development of the simulated tangential wind maximum.

c. Diagnosis of tangential velocity tendency equation

In cylindrical coordinates based at the center of circulation, the local time rate of change of azimuthally averaged tangential velocity can be written as

$$\frac{\partial \langle v \rangle}{\partial t} = -\langle u \rangle \langle \zeta_a \rangle - \langle w \rangle \frac{\partial \langle v \rangle}{\partial z} - \langle u' \zeta_a' \rangle - \left\langle w' \frac{\partial v'}{\partial z} \right\rangle - \left\langle \frac{1}{\rho} \frac{\partial p'}{\partial \lambda} \right\rangle + \langle F \rangle, \quad (4)$$

where $\zeta_a = f + (1/r)\partial(r\langle v \rangle)/\partial r$ is the azimuthal-mean vertical component of absolute vorticity. The rest of the symbols are as defined previously. On the right-hand side of Eq. (4), the first two terms represent the mean radial flux of mean absolute vorticity and the mean vertical advection of $\langle v \rangle$; the next two terms represent their eddy counterparts—namely, the eddy radial vorticity flux and the eddy vertical advection of eddy tangential momentum. The fifth term represents the azimuthal perturbation pressure gradient force per unit mass and the last term ($\langle F \rangle$) represents the combined effects of surface friction and subgrid-scale diffusion.

Figure 5 shows the terms of Eq. (4) for a calculation centered on hour 23, which is the time just prior to the establishment of the secondary tangential wind maximum near the top of the boundary layer (cf. Fig. 1). The term not shown is the azimuthal average of the azimuthal perturbation pressure gradient force per unit mass, which is much smaller than the other terms because of the small variation in the density with the azimuth. The figure shows the combined contribution of the two mean terms (Fig. 5a), the combined eddy terms (Fig. 5b), the local mean tangential velocity tendency (Fig. 5c), and the residual (Fig. 5d). The residual is calculated solving Eq. (4) for $\langle F \rangle$.

Figure 5 summarizes the contributions to the averaged tangential wind tendency for both the spin-down of the primary eyewall and the spin-up of the secondary eyewall. The present discussion will focus on the spin-up of the secondary eyewall by highlighting the various contributions to the tendency in the radial region of the SEF, located roughly between about 75- and 150-km radius. In the lowest part of the domain between about 75 and 150 km (Fig. 2f), mean tangential wind velocity change achieves values of about $1 \text{ m s}^{-1} \text{h}^{-1}$ (Fig. 5c). This acceleration is the result of the substantially larger and opposing contributions of different terms in the tangential velocity budget. The terms with the largest magnitudes are the combined mean terms (Fig. 5a) and

⁶ In the RAMS output, the friction term is not readily available and so the residual serves as an estimate of the frictional force per unit mass. This term contains not only the effect of frictional forces, but also inaccuracies associated with the interpolation from the staggered Arakawa C grid (in the Cartesian coordinates of the RAMS simulation) to the cylindrical coordinate grid used in the diagnostic analyses.

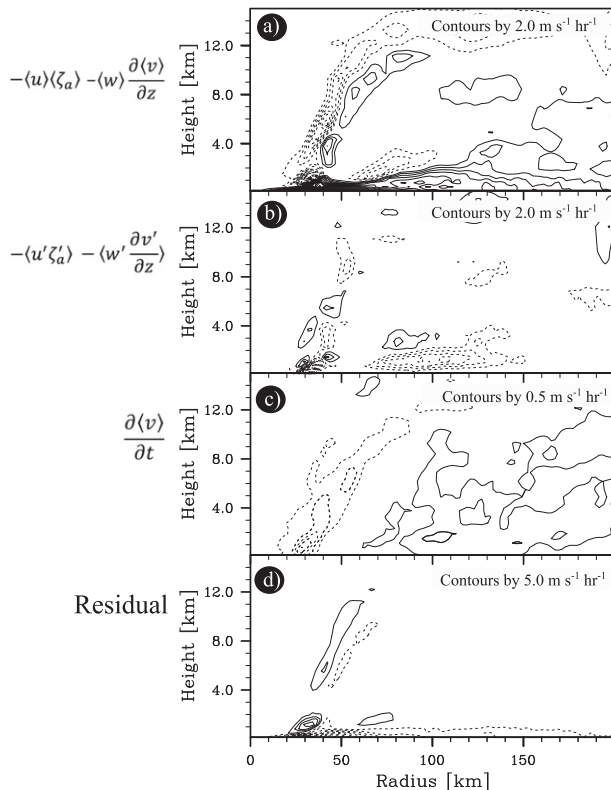


FIG. 5. The 2-h average of the terms in the tangential momentum equation centered around hour 23 from the mesoscale simulation. The terms shown are (a) the combined contribution of the mean radial vorticity flux and the mean vertical advection of mean tangential momentum, (b) the combined contribution of the perturbation radial eddy vorticity flux and the perturbation vertical advection of perturbation tangential momentum, (c) the local time change of tangential velocity, and (d) the residual, estimated as the difference between (c) and the sum of (a) and (b). For clarity, contours are shown every $2 \text{ m s}^{-1} \text{ h}^{-1}$ in (a),(b), $0.5 \text{ m s}^{-1} \text{ h}^{-1}$ in (c), and $5 \text{ m s}^{-1} \text{ h}^{-1}$ in (d). The zero contour is not shown.

the residual (Fig. 5d). The residual is associated with nonconservative effects owing to surface friction in the azimuthal direction, and is maximized in the frictionally boundary layer near the surface.

The combined mean terms (Fig. 5a) contribute to a positive tendency mainly below 2 km and between about 60- and 150-km radius. By definition, the mean advection terms are the sum of both the radial flux of mean absolute vorticity and the mean vertical advection of $\langle v \rangle$. In the boundary layer, the largest values of these two terms arise from the radial influx of mean absolute vorticity and this influx exceeds $30 \text{ m s}^{-1} \text{ h}^{-1}$ (not shown). The mean vertical advection of $\langle v \rangle$ attains values of more than $-10 \text{ m s}^{-1} \text{ h}^{-1}$ (not shown) and serves to loft the enhanced tangential wind generated in the boundary layer to the vortex aloft. The mean vertical advection term thus serves as a negative tendency

“sink” in the boundary layer and a positive tendency “source” in the vortex aloft between 1- and 2-km height.

In the SEF region, the combined effect of the eddy terms to the tangential wind tendency is small overall and negative in the boundary layer (Fig. 5b). Examining the individual components of the eddy terms (not shown), we find that the eddy radial flux of eddy absolute vorticity in the region of SEF is largely negative. On the other hand, the vertical eddy advection of eddy tangential momentum accounts for a negative tangential wind tendency below 2 km and a positive tendency above that height. The latter thus contributes to a spinup of the tangential wind above the boundary layer.

The foregoing results demonstrate that the actual SEF tangential velocity tendency in the SEF region occurs within but near the top of the boundary layer even in the presence of a strong spindown tendency associated with surface friction. The results show that the dominant contribution to the spinup of the mean tangential wind is associated with the mean radial influx of absolute vorticity in the boundary layer of the vortex. The results indicate also that in the region of SEF the main effect of the eddy vertical advection is to redistribute $\langle v \rangle$, serving to spin down $\langle v \rangle$ in the lowest 1 or 2 km and to spin up $\langle v \rangle$ in a layer above that. Together, these findings confirm the operation of the boundary layer spinup mechanism in the region of SEF as foreshadowed in the introduction.

Although the foregoing results provide strong support for the new boundary layer control hypothesis, a lingering question remains as to whether there is a clear causal link between the boundary layer dynamics and SEF.

d. Causality and the arrow of time

Figure 6 shows the time evolution of the tangential wind velocity, the horizontal divergence and the age-gradient force within the boundary layer at the model-level height of 457 m.⁷ For each quantity presented, both eyewalls are recognizable as independent maxima. The primary eyewall is centered between 25- and 30-km radius and the SE, which becomes increasingly clear with time, exhibits a radial contraction as described previously in Fig. 1.

⁷ Taking a boundary layer average of the lowest 962-m results in a figure consistent with Fig. 6, particularly in its space–time structure (not shown). The conclusions presented in this manuscript thus hold true with both approaches (i.e., single-level or layer-averaged views). The main difference between the two approaches is that the vertical average comprises larger subgradient wind magnitudes, which is to be expected because of the inclusion of the lowest levels that possess the largest deficit from the gradient flow at the boundary layer top.

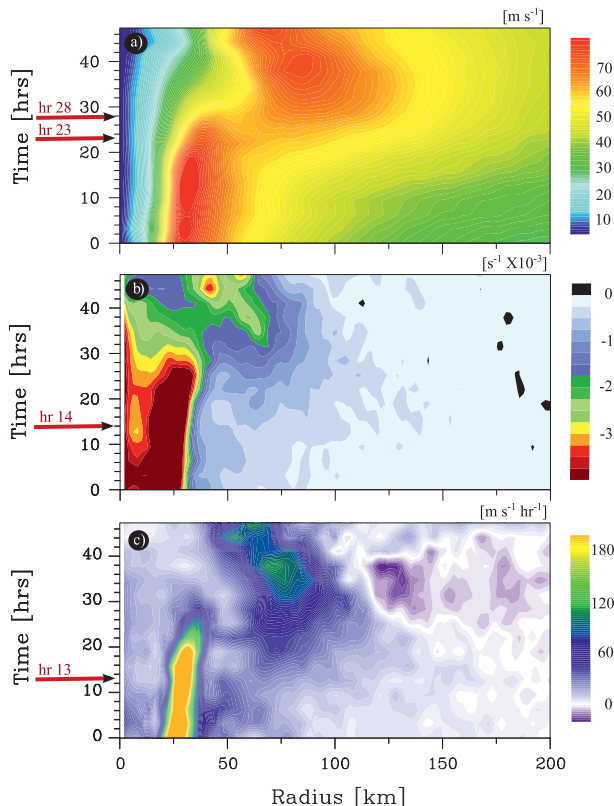


FIG. 6. Radius–time plot of azimuthal averages of (a) tangential wind velocity (m s^{-1}), (b) horizontal divergence ($\text{s}^{-1} \times 10^3$), and (c) agradient force ($\text{m s}^{-1} \text{ h}^{-1}$) at 457-m height from the mesoscale simulation. Color contours are plotted every $20 \text{ m s}^{-1} \text{ h}^{-1}$, $\text{s}^{-1} \times 10^3$, and 5 m s^{-1} , respectively. Red horizontal arrows and hour numbers indicate the earliest time that a secondary maximum of the plotted variable is discernible in the azimuthal average. [For reference, hour 23, the time of the earliest tangential velocity secondary maximum, at 1512 m (see Fig. 1) is indicated.]

Figure 6b shows the time evolution of horizontal divergence within the boundary layer. Horizontal convergence exhibits a secondary maximum in the boundary layer beginning around 14 h at 65-km radius and beginning around 15 h at 85-km radius. Recalling the chronological evolution presented in Figs. 1a, 2d–f, and 3a, the emergence of the convergence maximum precedes the emergence of the secondary tangential wind maximum at any height. The secondary convergence maximum at 85-km radius appears simultaneously with the secondary maximum in vertical velocity documented in Fig. 1. We will now show that although the secondary maximum in convergence and vertical velocity occur nearly simultaneously, their emergence is preceded by the maximum in the agradient force field.

Figure 6c presents the evolution of the agradient wind force field within the boundary layer. It shows that the

agradient force field develops a secondary maximum at hour 13 at 65-km radius and at hour 14 at 85-km radius. This secondary maximum precedes by 1 h the emergence of a secondary maximum in radial convergence and vertical velocity. Moreover, this secondary maximum in the agradient force field precedes by 10 h the emergence of the secondary tangential wind maximum (near the top of the boundary layer). This chain of events suggests strongly that the positive agradient force, which quantifies the effective outward radial force in the boundary layer, is the cause for the increased radial convergence and vertical motion on the system scale in the region of SEF. This sequence of events supports the idea that diagnostics of departures of gradient wind balance in the boundary layer may prove useful as a SEF forecasting tool (Huang et al. 2012). We look now for another test of the boundary layer control hypothesis using an independent modeling platform.

6. Further tests of the boundary layer control hypothesis using a simple slab model

In the previous sections it was shown that the emergence of the secondary wind maximum occurs near the top of the boundary layer and follows a chain of events initiated by a substantial radial expansion of the tangential wind field (associated with the first spinup mechanism) and the development of supergradient winds in the boundary layer (associated with the second spinup mechanism). The analysis of the SEF kinematics and dynamics in the RAMS simulation was thus shown to be consistent with the new SEF model developed by Huang et al. (2012), who proposed that the underlying boundary layer dynamics of a maturing hurricane vortex are an important controlling element in SEF. This idea is quite different from other SEF hypotheses summarized in the introduction. As with any new scientific idea, it should be tested from different perspectives. The authors of this manuscript are further testing the boundary layer control hypothesis using other full-physics hurricane simulations as well as observational datasets. The results of these analyses will be reported in due course. Here, we offer a complimentary approach for testing the proposed relationship between boundary layer dynamics and SEF.

The test is a relatively simple one: If SEF is largely a boundary layer response to a radially growing tangential wind field, one would expect that a boundary layer model would respond suitably in generating a secondary wind maximum using a fixed, simulated tangential wind field above the boundary layer in the full-physics model, together with reasonable estimates of the drag coefficient, the boundary layer depth, and horizontal eddy diffusivity.

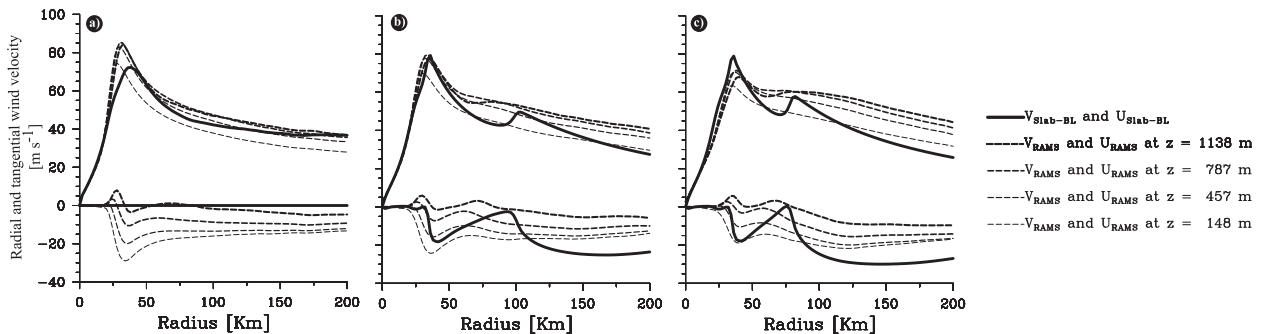


FIG. 7. Tangential and radial wind field profiles of the mesoscale simulation after azimuthal and 2-h averages at the $z = 1138$ -, 787 -, 457 -, and 148 -m model levels (dashed curves) and slab boundary layer simulations (instantaneous fields, solid black curves). (a) Wind profiles at hour 13 of the mesoscale simulation including the tangential wind profile at $z = 1512$ m that is used as the initial condition for the slab model and forcing (solid curve; see text for details). (b) Mesoscale model profiles centered at hour 18 and the results of the slab model (solid curve) after 5 h of integration. (c) Mesoscale model profiles centered at hour 23 and the results of the slab model (solid curve) at 10 h of integration, when the slab model is reaching equilibrium.

To execute such a test we integrate the slab boundary layer model described in section 2b, using as initial condition the RAMS azimuthally averaged tangential wind profile at the top of the boundary layer. The wind field is taken at hour 13, prior to the time that SE is evident in any of the azimuthally averaged fields of Fig. 1. We then compare the results of the RAMS and slab boundary layer models. To illustrate how the slab model typically achieves the computed equilibrium, radial profiles of the tangential and radial velocity are shown at the slab model times of 5 and 10 h. The solid curves in Figs. 7b and 7c show the temporal evolution of the slab boundary layer model, which reaches an equilibrium at about hour 11 of the integration. For reference, these outputs are compared with the 5-h output-interval data from the RAMS simulation centered at hours 13, 18, and 23 (dashed lines; Figs. 7a–c, respectively) using an azimuthal and 2-h average of the tangential and radial wind velocities at $z = 1138$ -, 787 -, 457 -, and 148 -m model levels, respectively. Also shown in Fig. 7a is the initially zero radial inflow⁸ and correspondingly averaged tangential wind from the RAMS simulation at $z = 1.512$ km, both of which were used to integrate the slab boundary layer model forward in time (dark solid curves).

Figure 7 shows that the slab boundary layer develops a secondary maximum in the tangential wind field. It shows also that such a maximum is not qualitatively unlike that found in the RAMS simulation. Figure 7b demonstrates that the secondary tangential wind maximum

in both models emerges clearly after only 5 h of numerical integration beyond 13 h (the initial condition of the slab boundary layer integration). At the time shown in Fig. 7b, the secondary tangential wind maximum in the slab model is centered at 105 km and reaches a value of 50 m s^{-1} . The RAMS secondary tangential wind maximum is centered at about 85 km with a magnitude of 55 m s^{-1} at $z = 1.138$ km. As in the typical evolution of eyewall replacement cycles (e.g., Willoughby et al. 1982; Willoughby and Black 1996), the secondary tangential wind maximum in both models becomes more pronounced with time as this feature contracts radially. At the time of Fig. 7c, the slab boundary layer tangential wind maximum attains a maximum value of 58 m s^{-1} , centered at 80-km radius. The RAMS tangential wind maximum reaches a value of 60 m s^{-1} at 80-km radius. Figures 7b and 7c show that, as in the case of the tangential wind, the radial velocity of the slab boundary layer model is qualitatively consistent with the corresponding radial profiles of the radial velocity found in the RAMS simulation. Both models exhibit radial inflow with two maxima, and each maximum resides just outside the corresponding tangential wind maximum.

The development of a secondary wind maximum is found to be a robust feature in the slab boundary layer model. This has been verified with a variety of sensitivity experiments using initial conditions and tangential-wind forcing taken from different vertical levels and times around hour 13 of the RAMS simulation (not shown). In all experiments conducted, the secondary tangential wind maximum emerges consistently with comparable magnitudes and radial location. These sensitivity experiments demonstrate that given a prescribed tangential wind field at the top of the boundary layer and reasonable estimates of the surface drag coefficient, radial eddy diffusivity,

⁸ Integrations of the slab boundary layer model initialized with the radial inflow from the RAMS simulation exhibit a very similar evolution to those initialized with zero radial inflow after the first hour or so when a rapid inertial adjustment of the inflow occurs.

and boundary layer depth, axisymmetric boundary layer dynamics alone are capable of developing a secondary tangential wind maximum and a concomitant region of focused convergence.

Although the boundary layer tangential and radial velocities in the two models exhibit qualitative consistency, there are quantitative differences among them. In the slab model, for example, the tangential wind maximum and its corresponding radial wind structure are somewhat more pronounced than in the RAMS model. Also, the tangential wind maximum in the slab model has a more localized secondary tangential wind maximum than that of the RAMS model. However, given the high degree of idealization invoked in the slab boundary layer model and its intrinsic limitations (e.g., Smith and Vogl 2008), quantitative differences between the models are to be expected.

The imposition of a fixed tangential wind profile prior to the emergence of the simulated tangential wind maximum is not necessarily the most accurate way to emulate the changing wind field above and within the boundary layer during the SEF process. However, this methodology has shown that a secondary tangential wind maximum can emerge solely as a result of boundary layer dynamics. Furthermore these experiments produced an unexpected result; namely, the simulated secondary wind maximum contracts inwards, as secondary eyewalls in mesoscale simulations and in nature do. Specifically, the inward contraction of the secondary wind maximum in the slab model occurs without special constraints on the underlying surface heat fluxes or special inertial stability considerations on the balanced secondary circulation above the boundary layer (cf. Emanuel 1994, 1997; Nong and Emanuel 2003; Schubert and Hack 1982)—properties that are irrelevant to the slab boundary layer model used here. These findings are interesting because they point to a hitherto unrecognized role of unbalanced boundary layer dynamics in the inward contraction of the outer eyewall under an imposed wind field at the boundary layer top.

7. Summary

In this paper we have sought to obtain an improved understanding of secondary eyewall formation by a careful analysis of the phenomenon in two different modeling frameworks. The first of them is a high-resolution, full-physics, three-dimensional mesoscale model in which we study an integration that undergoes a canonical eyewall replacement cycle. For this simulation, it is shown that secondary eyewall formation occurs in a region of the vortex where azimuthal averages of equivalent potential temperature and absolute angular momentum surfaces

are far from being congruent. This result questions the applicability of moist-neutral viewpoints and related mathematical formulations thereto for studying this process of tropical cyclone intensity change.

The analysis of the mesoscale simulation fully supports the recent findings of Huang et al. (2012). An investigation of the kinematics of secondary eyewall formation shows that the establishment of the secondary eyewall is the culmination of a sequence of structural changes in the tropical cyclone. The sequence begins with a radial broadening of the tangential wind field, followed by the emergence of persistent convective activity in the secondary eyewall formation's radial region, and subsequently followed by the emergence of the secondary wind maximum near the top of the boundary layer. An analysis of the dynamics of the secondary eyewall formation process confirms that the broadening of the tangential wind field above the boundary layer and the associated increase in the radial pressure gradient induces a boundary layer response that includes a relatively large radial inflow radially outside the primary eyewall. This strong inflow results in an outward-directed adiabatic force that causes sustained horizontal convergence. This convergence, in the conditionally unstable region where the secondary eyewall forms, leads to sustained deep convective activity. The strong inflow there results also in a strong mean influx of absolute vorticity that surpasses the depletion of absolute angular momentum by surface friction. When the radial inflow has attained sufficient strength, the net effect of the vorticity influx and frictional loss in the boundary layer is the generation of a secondary tangential wind maximum within the boundary layer outside the primary eyewall.

The second modeling framework is an axisymmetric, nonlinear, time-dependent, slab boundary layer model with radial diffusion. When this model is forced with the azimuthally averaged pressure field (associated with the gradient wind) at the top of the boundary layer from the mesoscale simulation at times well before the vortex exhibits a secondary wind maximum, the model generates a secondary tangential wind maximum. The secondary wind maximum is qualitatively comparable in both magnitude and time evolution to the maximum predicted by the mesoscale simulation. These results demonstrate that axisymmetric boundary layer dynamics alone are capable of developing secondary wind maxima. The results suggest also that unbalanced boundary layer dynamics may make an important quantitative contribution to the contraction of the tangential wind maximum.

Acknowledgments. The first author gratefully acknowledges the support from the National Research Council (NRC), through its Research Associateship

Program, and the host institution, the Naval Postgraduate School (NPS) in Monterey, California. The work was partially supported by the Office of Naval Research (ONR), through Award N0001411WX20095, and by the National Science Foundation (NSF) through Award AGS 0733380. The authors thank Timothy Dunkerton for the valuable discussion on the structure of equivalent potential temperature and absolute angular momentum and Roger Smith for his perceptive comments on the final draft of the manuscript. Finally, the authors thank Wesley Tervey for his guidance in the accessing of the mesoscale simulation data.

REFERENCES

- Abarca, S. F., and K. L. Corbosiero, 2011: Secondary eyewall formation in WRF simulations of Hurricanes Rita and Katrina (2005). *Geophys. Res. Lett.*, **38**, L07802, doi:10.1029/2011GL047015.
- Bell, M. M., and M. T. Montgomery, 2008: Observed structure, evolution, and potential intensity of category 5 Hurricane Isabel (2003) from 12 to 14 September. *Mon. Wea. Rev.*, **136**, 2023–2046.
- , —, and K. A. Emanuel, 2012a: Air–sea enthalpy and momentum exchange at major hurricane wind speeds observed during CBLAST. *J. Atmos. Sci.*, **69**, 3197–3222.
- , —, and W. C. Lee, 2012b: An axisymmetric view of concentric eyewall evolution in Hurricane Rita (2005). *J. Atmos. Sci.*, **69**, 2414–2432.
- Black, P. G., and Coauthors, 2007: Air–sea exchange in hurricanes: Synthesis of observations from the Coupled Boundary-Layer Air–Sea Transfer experiment. *Bull. Amer. Meteor. Soc.*, **88**, 357–374.
- Bogner, P. B., G. M. Barnes, and J. L. Franklin, 2000: Conditional instability and shear for six hurricanes over the Atlantic Ocean. *Wea. Forecasting*, **15**, 192–207.
- Bolton, D., 1980: The computation of equivalent potential temperature. *Mon. Wea. Rev.*, **108**, 1046–1053.
- Bui, H. H., R. K. Smith, M. T. Montgomery, and J. Peng, 2009: Balanced and unbalanced aspects of tropical-cyclone intensification. *Quart. J. Roy. Meteor. Soc.*, **135**, 1715–1731.
- Carrier, G. F., 1971a: The intensification of hurricanes. *J. Fluid Mech.*, **49**, 145–158.
- , 1971b: Swirling flow boundary layers. *J. Fluid Mech.*, **49**, 133–144.
- Clark, T. L., and R. D. Farley, 1984: Severe downslope windstorm calculations in two and three spatial dimensions using anelastic grid nesting: A possible mechanism for gustiness. *J. Atmos. Sci.*, **41**, 329–350.
- Cotton, W. R., and Coauthors, 2003: RAMS 2001: Current status and future directions. *Meteor. Atmos. Phys.*, **82**, 5–29.
- Drennan, W. M., J. A. Zhang, J. R. French, C. McCormick, and P. B. Black, 2007: Turbulent fluxes in the hurricane boundary layer. Part II: Latent heat fluxes. *J. Atmos. Sci.*, **64**, 1103–1115.
- Emanuel, K. A., 1986: An air–sea interaction theory for tropical cyclones. Part I: Steady-state maintenance. *J. Atmos. Sci.*, **43**, 585–604.
- , 1994: *Atmospheric Convection*. Oxford University Press, 592 pp.
- , 1995: Sensitivity of tropical cyclones to surface exchange coefficients and a revised steady-state model incorporating eye dynamics. *J. Atmos. Sci.*, **52**, 3969–3976.
- , 1997: Some aspects of inner-core dynamics and energetics. *J. Atmos. Sci.*, **54**, 1014–1026.
- , 2004: Tropical cyclone energetics and structure. *Atmospheric Turbulence and Mesoscale Meteorology*, E. Fedorovich, R. Rotunno, and B. Stevens, Eds., Cambridge University Press, 165–192.
- French, J. R., W. M. Drennan, J. A. Zhang, and P. B. Black, 2007: Turbulent fluxes in the hurricane boundary layer. Part II: Momentum fluxes. *J. Atmos. Sci.*, **64**, 1089–1102.
- Fudeyasu, H., and Y. Wang, 2011: Balanced contribution to the intensification of a tropical cyclone simulated in TCM4: Outer-core spinup process. *J. Atmos. Sci.*, **68**, 430–449.
- Hack, J. J., and W. H. Schubert, 1986: Nonlinear response of atmospheric vortices to heating by organized cumulus convection. *J. Atmos. Sci.*, **43**, 1559–1573.
- Harrington, J. Y., 1997: The effects of radiative and microphysical processes on simulated warm and transitional season arctic stratus. Ph.D. dissertation, Colorado State University, 289 pp.
- Hawkins, H. F., and S. M. Imbembo, 1976: The structure of a small, intense hurricane Inez 1966. *Mon. Wea. Rev.*, **104**, 418–442.
- Hendricks, E. A., M. T. Montgomery, and C. A. Davis, 2004: On the role of “vortical” hot towers in formation of tropical cyclone Diana (1984). *J. Atmos. Sci.*, **61**, 1209–1232.
- Hill, G. E., 1974: Factors controlling the size and spacing of cumulus clouds as revealed by numerical experiments. *J. Atmos. Sci.*, **31**, 646–673.
- Houze, R. A., Jr., S. S. Chen, B. F. Smull, W. C. Lee, and M. M. Bell, 2007: Hurricane intensity and eyewall replacement. *Science*, **315**, 1235–1239.
- Huang, Y. H., M. T. Montgomery, and C. C. Wu, 2012: Concentric eyewall formation in Typhoon Sinlaku (2008). Part II: Axisymmetric dynamical processes. *J. Atmos. Sci.*, **69**, 662–674.
- Jordan, C. L., 1958: Mean soundings for the West Indies area. *J. Meteor.*, **15**, 91–97.
- Judt, F., and S. S. Chen, 2010: Convectively generated potential vorticity in rainbands and formation of the secondary eyewall in Hurricane Rita of 2005. *J. Atmos. Sci.*, **67**, 3581–3599.
- Kossin, J. P., and M. Sitkowski, 2009: An objective model for identifying secondary eyewall formation in hurricanes. *Mon. Wea. Rev.*, **137**, 876–892.
- Kuo, H.-C., L.-Y. Lin, C.-P. Chang, and R. T. Williams, 2004: The formation of concentric vorticity structures in typhoons. *J. Atmos. Sci.*, **61**, 2722–2734.
- , W. H. Schubert, C.-L. Tsai, and Y.-F. Kuo, 2008: Vortex interactions and barotropic aspects of concentric eyewall formation. *Mon. Wea. Rev.*, **136**, 5183–5198.
- Lilly, D. K., 1962: On the numerical simulation of buoyant convection. *Tellus*, **14**, 148–172.
- Louis, J. F., 1979: A parametric model of vertical eddy fluxes in the atmosphere. *Bound.-Layer Meteor.*, **17**, 187–202.
- Maclay, K. S., M. DeMaria, and T. H. Vonder Haar, 2008: Tropical cyclone inner-core kinetic energy evolution. *Mon. Wea. Rev.*, **136**, 4882–4898.
- Martinez, Y., G. Brunet, and M. K. Yau, 2010: On the dynamics of two-dimensional hurricane-like concentric rings vortex formation. *J. Atmos. Sci.*, **67**, 3253–3268.
- Menelaou, K., M. K. Yau, and Y. Martinez, 2012: On the dynamics of the secondary eyewall genesis in Hurricane Wilma (2005). *Geophys. Res. Lett.*, **39**, L04801, doi:10.1029/2011GL050699.
- Montgomery, M. T., and R. J. Kallenbach, 1997: A theory for vortex Rossby waves and its application to spiral bands and

- intensity changes in hurricanes. *Quart. J. Roy. Meteor. Soc.*, **123**, 435–465.
- , and R. K. Smith, 2013: Paradigms for tropical-cyclone intensification. *Aust. Meteor. Oceanogr. J.*, in press.
- , M. E. Nicholls, T. A. Cram, and A. B. Saunders, 2006: A vortical hot tower route to tropical cyclogenesis. *J. Atmos. Sci.*, **63**, 355–386.
- , S. V. Nguyen, and R. K. Smith, 2009: Do tropical cyclones intensify by WISHE? *Quart. J. Roy. Meteor. Soc.*, **135**, 1697–1714.
- Nguyen, V. S., R. K. Smith, and M. T. Montgomery, 2008: Tropical-cyclone intensification and predictability in three dimensions. *Quart. J. Roy. Meteor. Soc.*, **134**, 563–582.
- Nong, S., and K. Emanuel, 2003: A numerical study of the genesis of concentric eyewalls in hurricanes. *Quart. J. Roy. Meteor. Soc.*, **129**, 3323–3338.
- Ooyama, K. V., 1969: Numerical simulation of the life cycle of tropical cyclones. *J. Atmos. Sci.*, **26**, 3–40.
- Pielke, R. A., and Coauthors, 1992: A comprehensive meteorological modeling system—RAMS. *Meteor. Atmos. Phys.*, **49**, 69–91.
- Qiu, X., Z.-M. Tan, and Q. Xiao, 2010: The roles of vortex Rossby waves in hurricane secondary eyewall formation. *Mon. Wea. Rev.*, **138**, 2092–2109.
- Roll, H. U., 1965: *Physics of the Marine Atmosphere*. International Geophysical Series, Vol. 7, Academic Press, 426 pp.
- Rotunno, R., and K. A. Emanuel, 1987: An air–sea interaction theory for tropical cyclones. Part II: Evolutionary study using a nonhydrostatic axisymmetric numerical model. *J. Atmos. Sci.*, **44**, 542–561.
- Rozoff, C. M., D. S. Nolan, J. P. Kossin, F. Zhang, and J. Fang, 2012: The roles of an expanding wind field and inertial stability in tropical cyclone secondary eyewall formation. *J. Atmos. Sci.*, **69**, 2621–2643.
- Sanger, N. T., M. T. Montgomery, R. K. Smith, and M. M. Bell, 2013: An observational study of tropical cyclone spinup in Supertyphoon Jangmi (2008) from 24 to 27 September. *Mon. Wea. Rev.*, in press.
- Schubert, W. H., and J. J. Hack, 1982: Inertial stability and tropical cyclone development. *J. Atmos. Sci.*, **39**, 1687–1697.
- Shapiro, L. J., 1983: The asymmetric boundary layer flow under a translating hurricane. *J. Atmos. Sci.*, **40**, 1984–1998.
- , and H. Willoughby, 1982: The response of balanced hurricanes to local sources of heat and momentum. *J. Atmos. Sci.*, **39**, 378–394.
- Sitkowski, M., J. P. Kossin, C. M. Rozoff, and J. A. Knaff, 2012: Hurricane eyewall replacement cycle thermodynamics and the relict inner eyewall circulation. *Mon. Wea. Rev.*, **140**, 4035–4045.
- Smagorinsky, J. S., 1963: General circulation experiments with the primitive equations. Part I: The basic experiment. *Mon. Wea. Rev.*, **91**, 99–164.
- Smith, R. K., 1968: The surface boundary layer of a hurricane. *Tellus*, **20**, 473–484.
- , and S. Vogl, 2008: A simple model of the hurricane boundary layer revisited. *Quart. J. Roy. Meteor. Soc.*, **134**, 337–351.
- , and M. T. Montgomery, 2010: Hurricane boundary-layer theory. *Quart. J. Roy. Meteor. Soc.*, **136**, 1665–1670.
- , and G. L. Thomsen, 2010: Dependence of tropical cyclone intensification on the boundary-layer representation in a numerical model. *Quart. J. Roy. Meteor. Soc.*, **136**, 1671–1685.
- , M. T. Montgomery, and S. V. Nguyen, 2009: Tropical cyclone spin-up revisited. *Quart. J. Roy. Meteor. Soc.*, **135**, 1321–1335.
- Terwey, W. D., and M. T. Montgomery, 2008: Secondary eyewall formation in two idealized, full-physics modeled hurricanes. *J. Geophys. Res.*, **113**, D12112, doi:10.1029/2007JD008897.
- , S. F. Abarca, and M. T. Montgomery, 2013: Comments on “Convectively generated potential vorticity in rainbands and formation of the secondary eyewall in hurricane Rita of 2005.” *J. Atmos. Sci.*, **70**, 984–988.
- Thomsen, G., M. T. Montgomery, and R. Smith, 2013: Sensitivity of tropical cyclone intensification to perturbations in the surface drag coefficient. *Quart. J. Roy. Meteor. Soc.*, doi:10.1002/qj.2048, in press.
- Walko, R. L., W. R. Cotton, J. L. Harrington, and M. P. Myers, 1995: New RAMS cloud microphysics parameterization. Part I: The single moment scheme. *Atmos. Res.*, **38**, 29–62.
- Willoughby, H. E., 1979: Forced secondary circulations in hurricanes. *J. Geophys. Res.*, **84** (C6), 3173–3183.
- , 1995: Mature structure and evolution. Global perspectives on tropical cyclones, World Meteorological Organization Tech. Doc. WMO/TD-693, 21–62.
- , and P. G. Black, 1996: Hurricane Andrew in Florida: Dynamics of a disaster. *Bull. Amer. Meteor. Soc.*, **77**, 543–549.
- , J. A. Clos, and M. G. Shoreibah, 1982: Concentric eye walls, secondary wind maxima, and the evolution of the hurricane vortex. *J. Atmos. Sci.*, **39**, 395–411.
- , F. D. Marks Jr., and R. J. Feinberg, 1984: Stationary and propagating convective bands in asymmetric hurricanes. *J. Atmos. Sci.*, **41**, 3189–3211.
- Wu, C.-C., Y.-H. Huang, and G.-Y. Lien, 2012: Concentric eyewall formation in Typhoon Sinlaku (2008). Part I: Assimilation of T-PARC data based on the ensemble Kalman filter (EnKF). *Mon. Wea. Rev.*, **140**, 506–527.
- Zhang, D.-L., Y. Liu, and M. K. Yau, 2001: A multiscale numerical study of Hurricane Andrew (1992). Part IV: Unbalanced flows. *Mon. Wea. Rev.*, **129**, 92–107.
- Zhang, J. A., and M. T. Montgomery, 2012: Observational estimates of the horizontal eddy diffusivity and mixing length in the low-level region of intense hurricanes. *J. Atmos. Sci.*, **69**, 1306–1316.
- , P. G. Black, J. R. French, and W. M. Drennan, 2008: First direct measurements of enthalpy fluxes in the hurricane boundary layer: The CBLAST result. *Geophys. Res. Lett.*, **35**, L14813, doi:10.1029/2008GL034374.
- Zhou, X., and B. Wang, 2011: Mechanism of concentric eyewall replacement cycles and associated intensity change. *J. Atmos. Sci.*, **68**, 972–988.
- , —, X. Ge, and T. Li, 2011: Impact of secondary eyewall heating on tropical cyclone intensity change. *J. Atmos. Sci.*, **68**, 450–456.